Delft University of Technology

Airfoil-Turbulence Interaction Noise Source Identification and Reduction by Leading-Edge Serrations

Bampanis, G.; Roger, M.; Ragni, Daniele; Avallone, Francesco; Teruna, Christopher

Important note
To cite this publication, please use the final published version (if applicable).
Please check the document version above.

Airfoil-Turbulence Interaction Noise Source Identification and Reduction by Leading-Edge Serrations

G.Bampanis[*], M.Roger[†], D.Ragni[‡], F.Avallone[§] and C.Teruna[¶]

École centrale de Lyon, 36 Avenue Guy de Collongue, 69134 Écully, France
Delft University of Technology, AWEP Dept., Kluyverweg 1, 2629HS

The present work is aimed at assessing leading-edge serrations as an airfoil turbulence-impingement noise (TIN) reduction mean. It relies on extended anechoic wind-tunnel testing including far-field measurements over an observation sphere to infer the three-dimensional features of TIN, and on microphone-array measurements to extract leading-edge noise in frequency. In particular this allows measuring unambiguously reductions of up to 15 dB achieved by serrations on flat plates. A preliminary study of the three-dimensional flow field around the leading edge using time-resolved tomographic particle image velocimetry (PIV) is detailed.

Introduction

Turbulent flows interacting with solid surfaces are efficient sources of broadband noise. In particular the turbulence-impingement noise (TIN) generated at the leading edge of an airfoil placed in a highly disturbed flow is considered a generic problem of primary engineering and research interest. Numerous applications are found in many engineering domains, such as low-speed fans in engine cooling units or in ventilation systems, wind turbines and propulsive rotating-blade technologies for aeronautical transport, drones and so on. Typically, a protection grid or a heat exchanger upsteam of a cooling fan, the rotor wakes of the fan of a turbofan engine impinging on outlet guide vanes or just atmospheric turbulence are sources of broadband noise for rotating blades or stationary vanes that cannot be easily mitigated without affecting the design parameters of the geometries. Therefore alternative sound-reduction strategies must be sought in modifications of the blades or vanes that remain compatible with the aerodynamic performances. In recent years several studies have been carried out on TIN reduction by modifying the material and mainly the geometry of the leading edge [1–3]. The present work is part of a research program dealing with both the effect of sinusoidal leading-edge serrations and the effect of porosity of some airfoil parts. It is the continuation of a preliminary study in which both technologies have been compared [4], with promising results in terms of noise reduction even with non-optimized implementation. The noise reduction mechanism originates from a destructive interference between the tips and roots of the serrations and from the rapid de-correlation of surface pressure fluctuations along the leading edge as the serration amplitude increases [5, 6]. A parametric study of a number of modified serrated LE profiles has been performed by [2, 3, 5, 7–12], for flat-plates and thick airfoils. The performances in terms of noise are simply obtained by comparing spectra with and without serrations. The pitch and depth of the serrations, the mean-flow speed and the turbulence length scale are the main parameters for understanding the noise reduction mechanisms. A recent study by [5] determines an optimum serration wavelength ensuring maximum TIN reduction. The maximum is obtained when one-fourth of the serration wavelength is approximately equal to the impinging turbulence integral length scale. It was shown that three-dimensional airfoils with similar geometrical features present a similar acoustic behavior after applying the optimum serration wavelength. In addition, a simple model based on the conclusions of reference [6] was proposed to the reduction in the far field as a function of the Strouhal number $St_h = fh/U_0$ based on the serration height h. Logically, leading-edge serrations of random shape have been later assessed, giving encouraging noise reductions [12]. Porosity applied on airfoils is another promising way of reducing TIN but few extensive studies exist till now [1, 4]. The action of porosity is presumably dealing with a compromize between actions of viscosity and compressibility inside the material. The feasibility of leading-edge serrations is strongly related to the main airfoil geometrical parameters that are the chord and the thickness. Serrations are more naturally suited to thin airfoils whereas porosity is more appropriate for

---

[*]PhD candidate, École centrale de Lyon, georgios.bampanis@ec-lyon.fr

[†]Professor, École centrale de Lyon, michel.roger@ec-lyon.fr

[‡]Assistant Professor, Faculty of Aerospace Engineering, Delft University of Technilogy, D.Ragni@tudelft.nl

[§]Assistant Professor, Faculty of Aerospace Engineering, Delft University of Technilogy, F.Avallone@tudelft.nl

[¶]PhD candidate, Faculty of Aerospace Engineering, Delft University of Technilogy, C.Teruna@tudelft.nl

thick airfoils because it requires a minimum available volume. Aforementioned works refer to sound measurements performed in the mid-span plane of a rectangular airfoil. For applications to rotating blades investigating the sound field off the mid-span plane is also necessary, though the dipole character of TIN sources makes it expectedly lower. This is one of the objectives of the present work, extending a previous preliminary study by the authors [13]. Furthermore previous works also pointed the masking effect of trailing-edge noise (TEN), which prevents the leading-edge noise to be convincingly accessible from simple far-field microphone measurements at high frequencies and/or for large reductions. In order to complete and extend the existing data base a two-step experimental approach has been carried out. As long as TIN remains dominant, which is the case in the low-and-medium frequency range, the reduction is deduced from the far-field measurements. In contrast at high frequencies for which TEN dominates, a near-field microphone array is used to produce some source localization maps from which the serration-induced reduction is directly estimated from the source strength. The setup and the airfoil design are described in section I.A. The alternative approach from array post-processing is described in section III. Section IV is devoted to the accompanying PIV experiment and the associated preliminary post-processing.

I. Experimental Set-up and airfoils design

A. Wind-Tunnel Setup

All acoustic measurements have been conducted in the low-speed anechoic open-jet wind tunnel of Ecole Centrale de Lyon (ECL). The overall dimensions of the anechoic room are 4 m x 5 m x 6 m and the whole setup is shown in Fig. 1. A rectangular nozzle with a vertical outlet cross-section of 15 cm x 30 cm delivers a uniform flow into the anechoic chamber with a speed ranging from 19 m/s to 32 m/s. In all tested configurations the turbulent flow is generated by a grid placed upstream of the nozzle contraction (cross-section 30 cm x 30 cm). The grid is made of thin flat bars of 8 mm width and 2 mm thickness, and it has a mesh size of 5 cm. The grid produces nearly homogeneous and isotropic turbulence, as confirmed by hot-wire measurements previously performed in absence of the airfoil at the location of the leading edge. A single hot-wire probe was used to this end. The turbulent intensity and the integral length scale have been found of 4.5% and 9 mm, respectively by fitting a model von Kármán spectrum on the measured streamwise velocity spectrum. All tested airfoils were held between two narrow supports which minimize sound reflection or masking and allow for far-field measurements in a wide range of oblique directions off the mid-span plane (Fig. 1). A rotating vertical arc of six microphones (B&K 1/2″ type 4189) is used to scan the three-dimensional radiating pattern of TIN on a portion of sphere, the measuring point being defined by its spherical coordinates (R, θ, ϕ). The microphones are equally distributed along the arc from $\phi = 0°$ (mid-span plane) to 75° by steps of 15°. Their distance to the airfoil leading-edge center point taken as origin is $R = 1.25$ m. The acquisition of the acoustic pressure has been made for the six microphones with an external unit $PXI − 1036$ averaging on 30 samples of 1 second, with the sampling frequency 51.2 kHz and a frequency resolution of 1 Hz. The arc is attached to one end of a horizontal bar, the other end of which is fixed on a vertical pylon aligned with the airfoil leading edge. The pylon is fixed on a rotating table, so that the angle θ of the meridian plane of the arc from the streamwise direction is varied between 20° and 110°. The limited angular ranges ensure that the measurements are neither contaminated by the hydrodynamic pressure of the wind-tunnel jet, nor distorted by sound scattering on the narrow supports. Yet spurious sound reflection/scattering occurs on the bar and on the inner face of the arc. The scattered field interferes with the direct field at the microphone locations but the associated interferences are eliminated by the spectral difference. An extended description of the set-up and instrumentation has been done by Bampanis *et al.* [13].
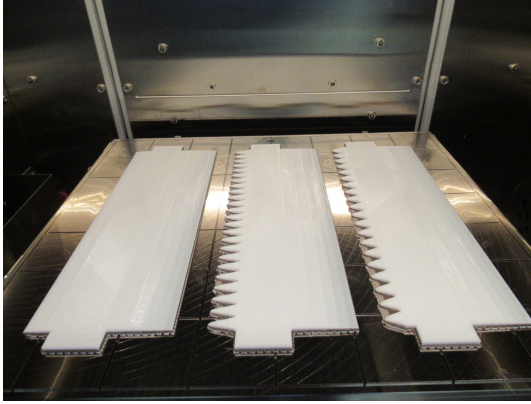
B. Flat-Plate Airfoils

A thin-airfoil design has been chosen, starting from flat plates. Two modified flat-plate airfoils with wavy leading edges and one baseline airfoil with straight leading edge have been manufactured with three-dimensional printing. The leading and the trailing edge are designed following the formula for a symmetric 4-digit NACA profile. More precisely the NACA shape has been split into two parts at its maximum thickness point and extended by including a constant-thickness flat-plate portion in between. The thickness is of 3 mm, with a wetted span of 30 cm equal to the nozzle height and a mean chord length of 10 cm, same for all designs. The serration profile is therefore symmetrical on both sides of the straight edge location. The corners of the leading-edge cuts have been improved surface regularity everywhere. This avoids both the additional vortex generation that would take place at the serration edges and the vortex-shedding sound associated with trailing-edge bluntness.

Fig. 1 Photograph of the setup showing the nozzle on the left, the installed airfoil (white rectangle) and the circular arc of microphones in the ECL anechoic chamber. The black multi-branched structure behind the airfoil is the microphone array used for source localization.

The parameters of the two serrated versions are *a priori* tuned to the integral length scale Λ of the incident turbulence, here measured as 9 *mm*, according to the observation by Chaitanya *et al.* [2] that efficient noise reduction depends on proper inclination angle and amplitude of the sinusoidal serrations. The airfoil with the longer serrations is expectedly close to the optimum design in that sense. It has dimensionless depth $h/c_0 = 0.167$ and inclination angle $\theta = 76°$. The smaller serrations are understood as a way of assessing sensitivity to the design. The baseline mock-up is considered as reference. The three flat-plate airfoils and the narrow-support installation are shown in Figs. 2-(a) and (b). It is noted that the zero angle of attack cannot be varied with the present setup. This is justified by the fact that TIN is nearly independent of that angle.
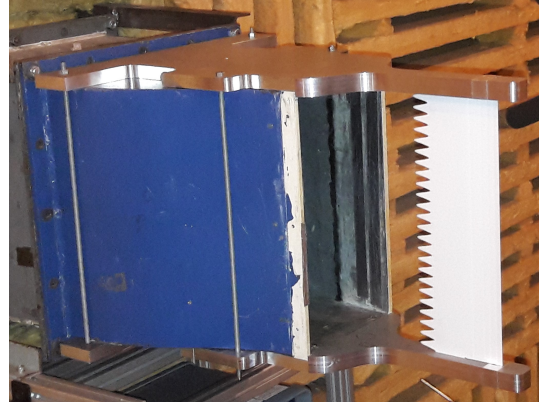
(a)   **(b)**

Fig. 2 Detailed pictures of the setup and tested flat-plate airfoils (a)Flat plates:baseline, large serrations and small serrations; (b) Nozzle and narrow supports.

II. Turbulence-Impingement Noise Investigation

Background-noise subtraction in the far-field provides an estimate of the noise radiated by the airfoil but it still combines TIN and TEN sources, the latter possibly masking the former at high frequencies. Therefore, additional efforts based on more advanced techniques are needed to isolate TIN and better understand the underlying physics. Some of these techniques are beamforming methods or similar based on the use of a microphone array. The first issue is to

isolate TIN in order to produce convincing reduction spectra over an extended frequency range by subtracting far-field sound spectra measured with and without the modifications. It is addressed in section A below. Refined estimates produced by an innovative use of microphone-array measurements are presented in section B. The identification of the background-noise sources is a necessary preliminary step. In the present installation, contributions to the background noise are the noise coming from the inserted grid upstream of the contraction inside the nozzle, the mixing noise of the jet and the noise produced by the flow on the edges of the nozzle and on the narrow supports. All must be eliminated by subtracting the sound measured without the airfoil from the total noise measured with the airfoil.

Once the aforementioned background-noise sources are eliminated the measured noise still includes the TIN of interest and the undesirable TEN. A second subtraction procedure could be defined to eliminate TEN, typically by repeating the measurements without turbulence grid in the nozzle to estimate TEN separately. A more relevant method is described in section III.

A. Differences of Far-Field Sound Spectra for Baseline and Serrated Airfoils

Far-field noise spectra for the three flat-plate airfoils are shown in Figs. 3-(a), (b) and (c) for three flow-speeds 19, 27 and 32 m/s, respectively, and the measurement angles $\phi = 0°$ and $\theta = 90°$. The background noise has been subtracted from all measurements and the data are reliable up to the threshold of 15 kHz, beyond which a larger scatter appears with the present resolution of $1Hz$. Sound level and frequency increase with flow speed as expected. Furthermore the spectra exhibit dips and humps attributed to the chordwise non-compactness. The serration-induced noise reduction is clearly seen in Fig. 3-(d) where spectra for the three airfoils are compared at the same speed. For further treatment the bandwidth resolution will be decreased to 16 Hz (Fig. 3) or 64 Hz (Fig. 4-(a)) for better clarity.

The reduction of TIN is defined as the quantity ΔSPL produced by the difference spectra. This quantity is plotted in Fig. 4-(a) for the three flow speeds. It exhibits different trends depending on the range of Strouhal number. A regular increase with frequency is first seen up to $St = 1.5$; then the reduction seems to drop and starts increasing again beyond $St = 2.5$. The high-frequency behavior is an artifact of the procedure, as discussed later on. Higher noise reductions are observed for the lower speeds 19 and 27 m/s below the Strouhal number $St = 1$ and beyond $St = 2.5$, with reversed behavior between these two values. Figure. 4-(b) shows far-field spectra at various speeds for the serrated airfoil with deepest serrations in reduced variables. The PSD of the acoustic pressure divided by flow speed to the power 5 plotted as a function of the Strouhal number produces a clear collapse, except beyond $St = 0.5$ because of the non-compactness dips and humps. This trend is characteristic of TIN, also for straight-edge airfoils.

(a)

(b)

(c)

(d)
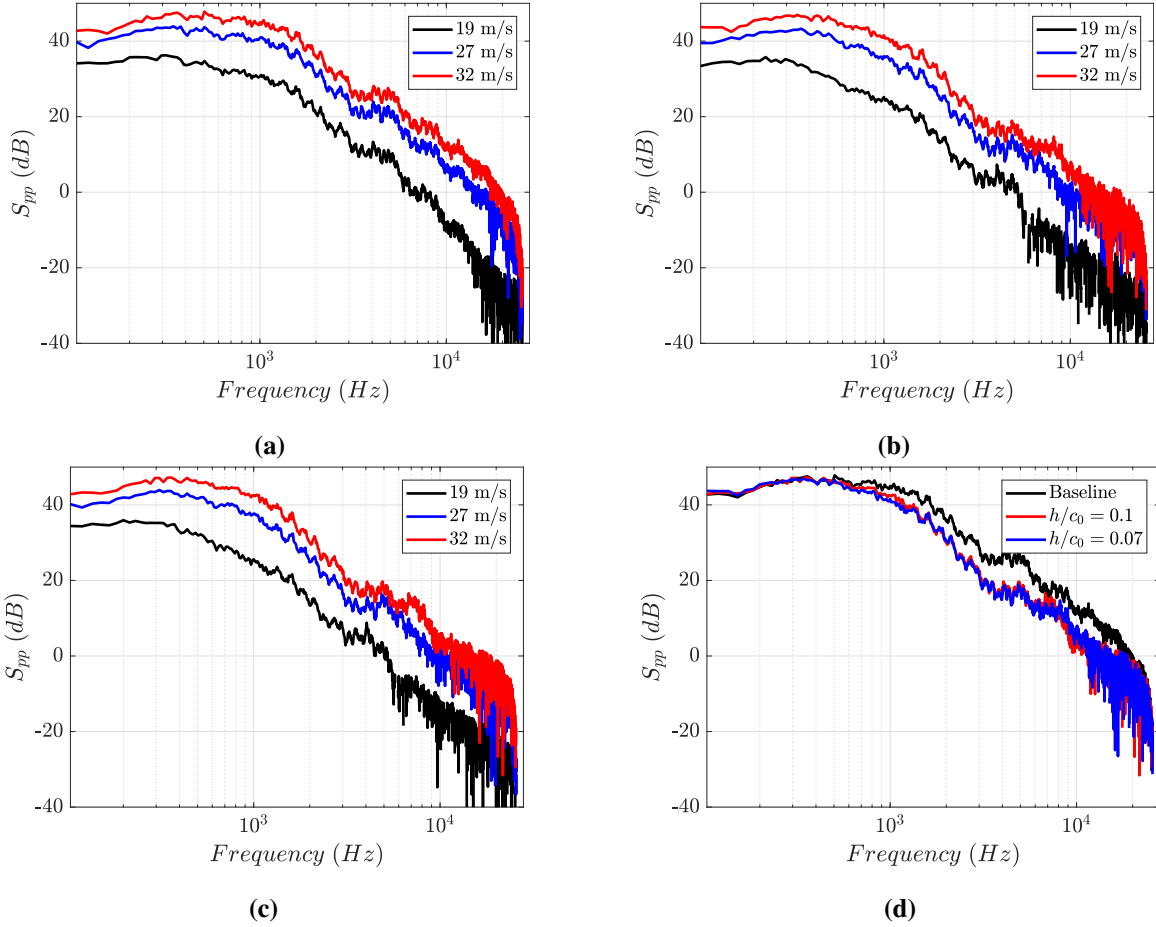
Fig. 3   Far-field sound spectra at various flow speeds. Microphone angles $\phi = 0°$, $\theta = 90°$. (a) baseline airfoil, (b) serrations h/c$_0$ = 0.07, (c) serrations h/c$_0$ = 0.1. (d) Compared sound spectra of the three airfoils at U = 32 m/s.

(a)

(b)
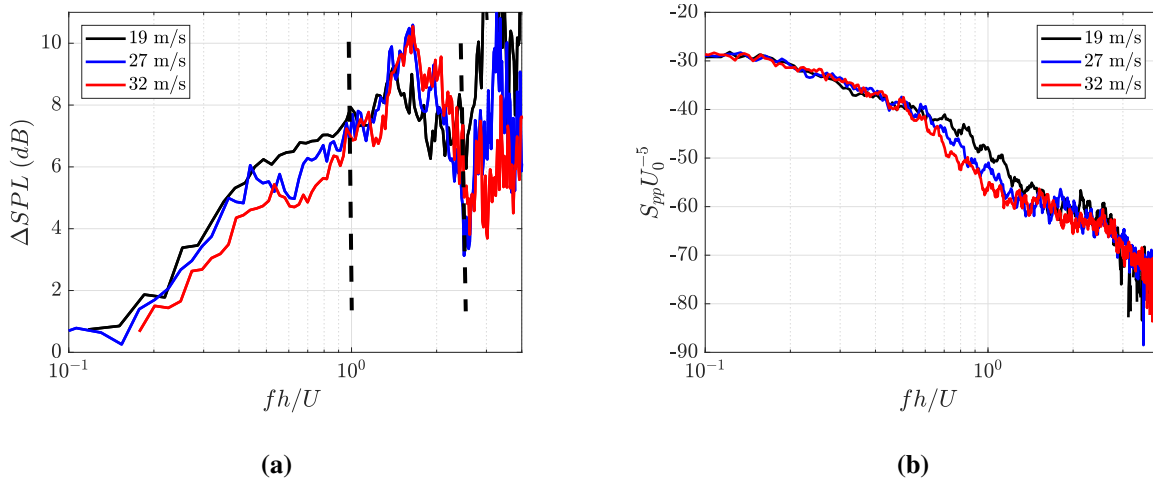
Fig. 4   (a) Noise reduction from far-field inspection, (b) Strouhal-number spectra scaling law with the 5th power of the flow speed radiation. Microphone angles $\phi = 0°$, $\theta = 90°$, serrated airfoil $h/c_0 = 0.1$.

As pointed in a previous study by the authors [13], making the difference in decibels between simple far-field sound spectra produces misleading reduction spectra at high frequency. This is responsible for the artifact noted in

5

Fig. 4-(a) and observed similarly in Fig. 5-(a) for a microphone at 90° in the mid-span plane (this location is chosen for further comparison with the microphone-array measurements of section III). In this figure the two serrated airfoils are compared. The reduction is found to be an increasing function of frequency up to a maximum of about 8-10 dB in the range 4-6 kHz. At higher frequencies a dramatic drop of reduction is found, followed by another increase. This is better understood by inspecting also the sound spectra corresponding to the total noise and to the selfnoise in Fig. 5-(b). Selfnoise is measured by removing the turbulence grid and forcing transition to turbulence in the boundary layers by tripping when needed. It is trailing-edge noise and takes over TIN for frequencies typically beyond 4 kHz. Indeed both spectra have levels close to each other and the same shape in this range. Furthermore subtracting the TEN spectrum (blue) from the total spectrum (red) would produce a PSD level lower than the TEN spectrum. This makes the simple subtraction procedure in Fig. 5-(a) inappropriate to evaluate the TIN reduction operating at the leading-edge. Apart from this differences between the two serrated flat-plate airfoils in terms of noise reduction are observed in Fig. 5-(a). The $h/c_0 = 0.1$ configuration ensures a larger reduction in the low frequency range than the $h/c_0 = 0.07$ configuration with shorter teeth.


(a)   **(b)**
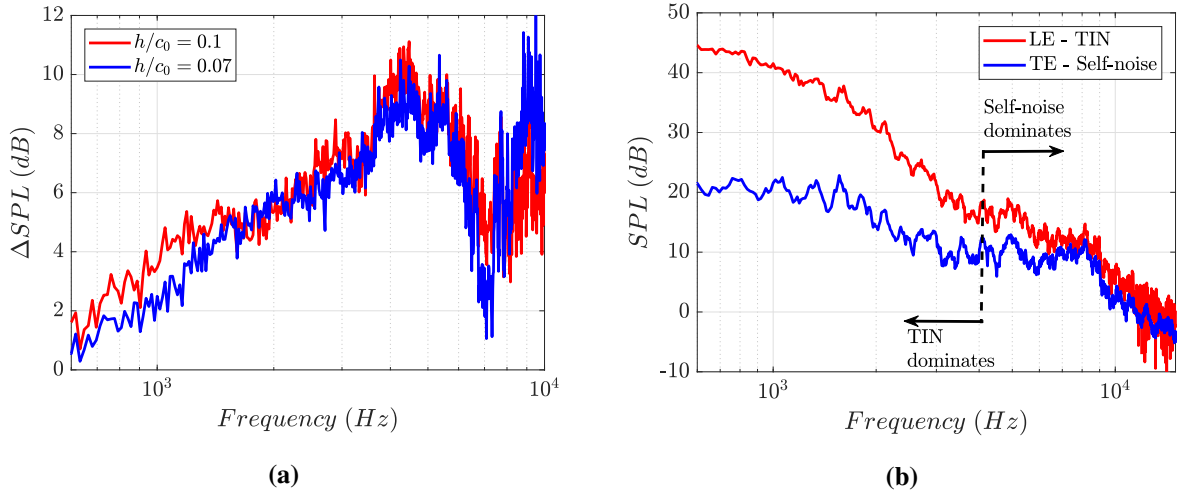
Fig. 5   (a) Noise-reduction spectra obtained for the serrated flat-plate airfoils by simple spectra subtraction and (b) typical far-field noise spectra comparing total noise (TIN+TEN) and TEN. Flow speed $U = 32m/s$, observation angle 90° in the mid-span plane.

B. Directivity Patterns and Comparison with Analytical Predictions

Cuts of the three-dimensional directivity of TIN are plotted for the baseline airfoil and the serrated airfoil with $h/c_0 = 0.1$ in Fig. 6, for a set of frequencies between 0.5 and 7.2 kHz. The plots are projections of the cuts in the plane of angle θ. The solid lines represent the acoustic radiation in the mid-span plane and the dotted lines those in the plane of elevation angle $\phi = 75°$. The large difference between the former and the latter is expected from the dipolar nature of the sources. As frequency increases, the dipole-like one-lobed radiation pattern evolves progressively to a three-lobed pattern. This is related to the chordwise airfoil non-compactness. Indeed the single-lobe shape for both airfoils is maintained below a threshold of about 3 kHz, 3.4 kHz corresponding to the value 2π of the Helmholtz number kc_0. Beyond this limit the airfoil becomes substantially non-compact. The radiation at the highest measured angle $\phi = 75°$ seems to keep the same one-lobe trend at all frequencies.

The small thickness of the flat-plate airfoils was initially chosen to ensure reliable comparisons with analytical models usually based on the zero-thickness assumption. In the present paper predictions have been made for the baseline airfoil only using Amiet's TIN model in the frequency domain. Only key features of the model are given; details can be found in the references below. The power spectral density of the far-field pressure is expressed as

$$S_{pp}(\boldsymbol{x}, \omega) = \left(\frac{\rho_0 kc\, x_3}{2S_0^2}\right)^2 \pi U \frac{L}{2} \Phi_{ww}(k_1, k_2) |\mathcal{L}(x_1, k_1, k_2)|^2 \tag{1}$$

6
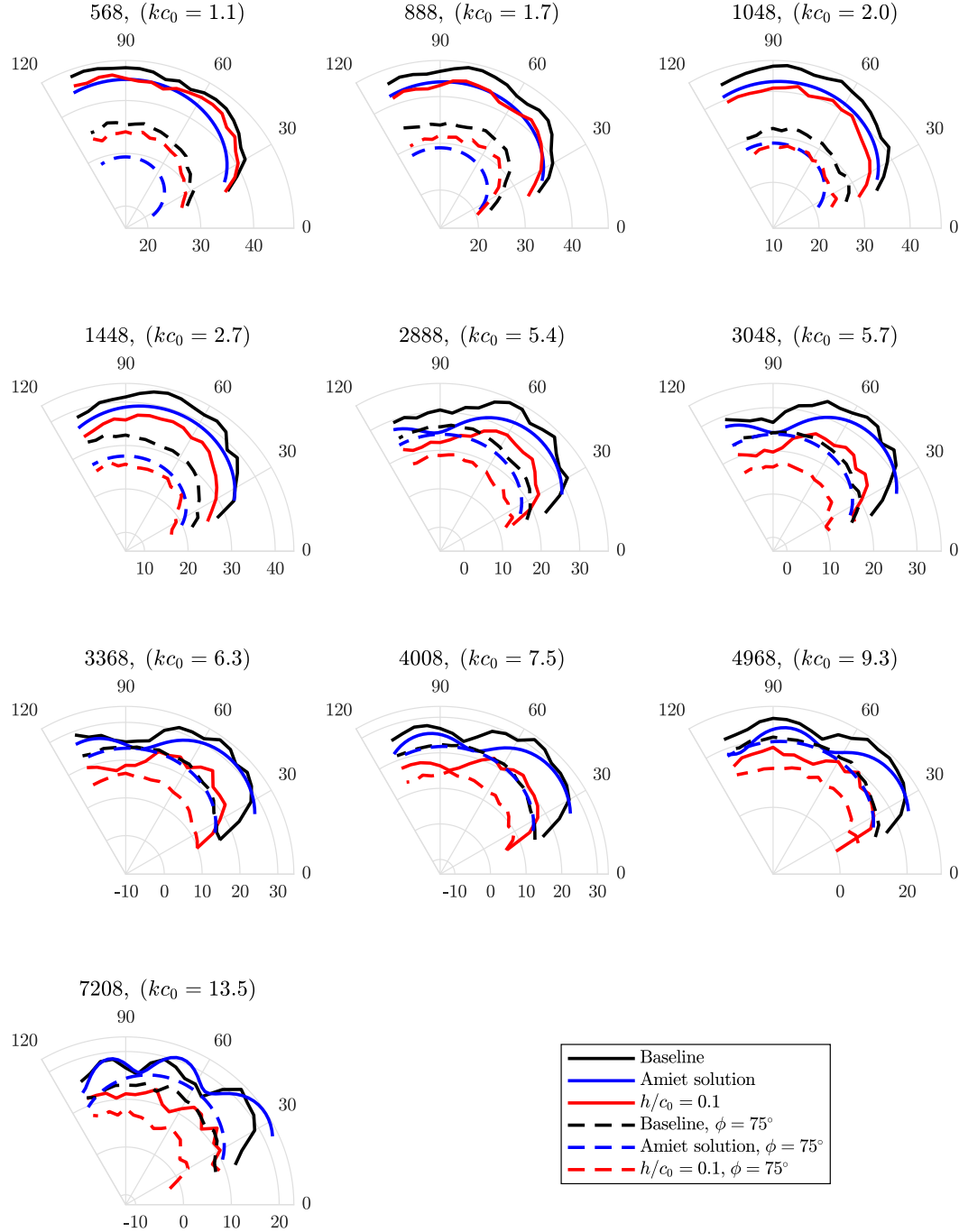
Fig. 6 **Far-field directivity polar diagrams measured at 32 m/s in the mid-span plane and in the horizontal plane corresponding to the last arc microphone. Frequencies in Hz and associated chord-based Helmholtz numbers kc_0. Red lines: serrated LE $h/c_0 = 0.1$, black lines: baseline, blue lines: predictions.**

where

$$S_0 = \sqrt{x_1^2 + \beta^2(x_2^2 + x_3^2)} \quad \text{with} \quad \beta = \sqrt{1 - M^2}, \quad M = U/c,$$

c being the sound speed.

Taylor's assumption of frozen incident turbulence is made. The turbulence is expanded by space Fourier analysis in oblique sinusoidal upwash components called gusts and defined by two wavenumbers k_x, k_y in the chordwise and

7

(a)   **(b)**
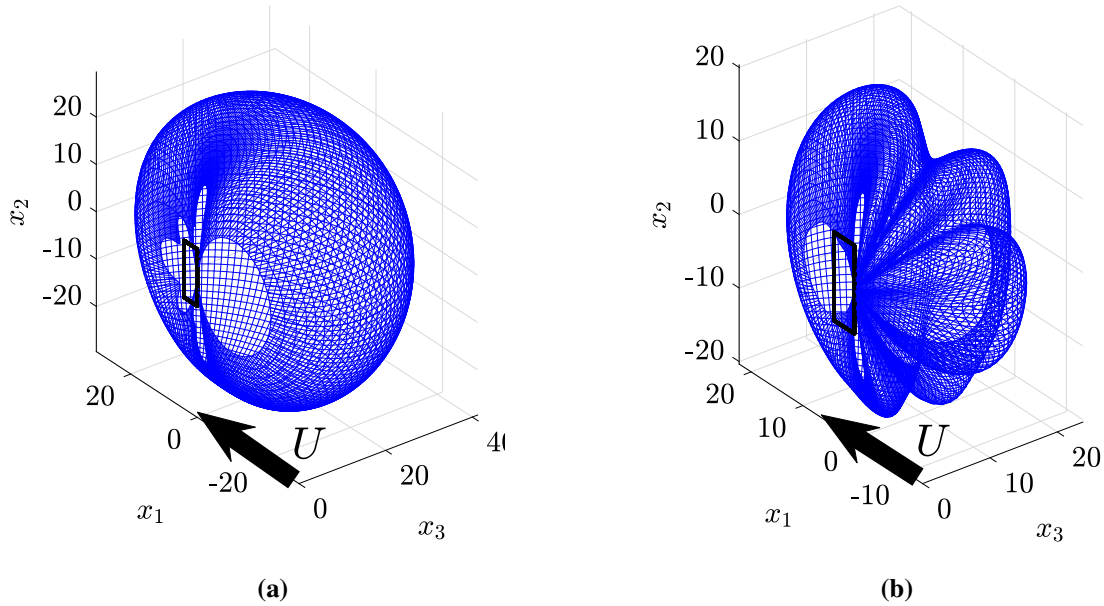
Fig. 7 Predicted 3D directivity of the TIN of the straight leading-edge flat-plate at Mach number $M = 0.09$ ($U = 32\,m/s$). Von Kármán model used as input with integral length scale $\Lambda = 0.009\,m$ and turbulent intensity 4.5 %. (a) $k\Lambda = 0.05$ and (b) $k\Lambda = 0.8$.

spanwise directions respectively. Its statistical properties are described by the two-dimensional wavenumber spectrum according to the Von Kármán model Φ_{ww}, expressed as

$$\Phi_{ww}(k_1, k_2) = \frac{4}{9\pi} \frac{\bar{u^2}}{k_e^2} \frac{\hat{k}_1^2 + \hat{k}_2^2}{(1 + \hat{k}_1^2 + \hat{k}_2^2)^{7/3}}, \tag{2}$$

where

$$\hat{k}_{1,2} = \frac{k_{1,2}}{k_e}, \qquad k_1 = \frac{\omega}{U}, \ k_2 = \frac{kx_2}{S_0}, \qquad k_e = \frac{\sqrt{\pi}}{\Lambda} \frac{\Gamma(5/6)}{\Gamma(1/3)},$$

Λ being the integral length scale and $\bar{u^2}$ the mean-square turbulent velocity, with

$$\sqrt{\bar{u^2}} = \frac{TI \cdot U}{100}$$

TI denoting the turbulent intensity. $\mathcal{L}$ is an analytical aeroacoustic tranfer function, sum of the main leading-edge scattering term $\mathcal{L}_1$ and the trailing-edge scattering term $\mathcal{L}_2$. It combines a theoretical expression for the spanwise distribution of the unsteady lift and a phase term accounting for propagation-path differences, both integrated from leading edge to trailing edge. In its most general form, the result should involve integration over all wavenumbers k_2 for a fixed wavenumber $k_1 = \omega/U$. The aeroacoustic tranfer functions $\mathcal{L}_1$ and $\mathcal{L}_2$ would have different expressions depending on the wavenumber vector (k_1, k_2) and corresponding to so-called supercritical and subcritical gusts [14, 15]. The general form is only needed for rectangular flat-plate airfoils of small aspect ratio L/c_0. For aspect ratios of about 3 and more, the asymptotic limit of large aspect ratio leading to Eq. (2) is accurate enough [14, 16]; it only involves the supercritical gusts of spanwise wavenumbers $k_2 = kx_2/S_0$. Typical three-dimensional directivity patterns of TIN as predicted using Amiet's theory are plotted in Fig. 7 for two frequencies corresponding to the dimensionless wavenumbers $k\Lambda = 0.05$ and $k\Lambda = 0.8$ based on the integral length scale, or $kc_0 = 0.56$ and $kc_0 = 8.9$ based on the chord length. At the lowest frequency the directivity is that of an equivalent compact dipole. At the highest frequency three lobes in the θ direction are identified, with increasing amplitude from upstream to downstream.

Theoretical directivity plots are reported in Fig. 6 as the blue solid lines for the microphone at $\phi = 0°$ and as the blue dashed lines for the microphone at $\phi = 75°$. The validity of the model was proved in the past regarding its application in

8

the mid-span plane but not off the mid-span plane. The present results indicate good performance in all directions, despite the fact that corrections were not implemented for the refraction of sound that occurs through the jet shear layers. These corrections are negligible for the present experiment. Independently of these effects Amiet's model underestimates the sound radiation at low frequencies.

Amiet's model based on Schwarzschild's technique cannot be applied to serrated airfoils. A recent alternative analytical model for serrated flat-plate airfoils has been developed by Ayton & Kim [17]. Because of the increased mathematical complexity this model only addresses the main leading-edge scattering, extending the solution $\mathcal{L}_1$, and does not consider a trailing-edge correction. As such it is expected valid for sufficiently high frequencies, which is not restrictive. Its implementation for comparison with the present results will be the mater of future work.

Going back to the experimental results in Fig. 6 reveals that the directivity is not essentially modified by the serrations. The same overall pattern is featured for the serrated airfoil as for the baseline airfoil [13]. The small directivity differences observed at the highest frequency can be attributed to the possible contamination by TEN. Solving the issues associated with this contamination is the matter of the next section.

III. Source Localization and Extraction

Advanced post-processing techniques of microphone arrays that extend the capabilities of conventional beamforming (CBF) can be used to extract and quantify the acoustic signature of one source from a total sound field in which several sources contribute. They have been recognized as a crucial need in the present work to solve the aforementioned high-frequency issues in the TIN studies associated with trailing-edge noise. Here the deconvolution algorithm called CIRA operated by LMS software has been used. It has been developed by ONERA in 1994 and is based on classical beamforming. A detailed description of the method is given by Piet *et al.* [18]. CIRA denotes a branch of advanced sound source localization algorithms which overcomes some of the significant drawbacks of conventional beamforming. The spatial resolution limits have been broadened, improving the performance at low frequencies. Therefore, the source identification and separation in case of several sources is made possible, as well as a relevant estimate of power-level spectra for each source. Again the reader will find details of the algorithms in the references. The technique is used as a tool in the present work and only practical implementation points are discussed. A previous application of the same method, using the same microphone array, and the comparison with other localisation techniques for airfoil-noise extraction is already described by Yakhina *et al.* [19].

In particular the low-frequency spatial resolution limit is evaluated from the condition $R_B/L_s \lesssim 0.5$, where $R_B \backsim R/D$ is the beamforming spatial resolution, L_s the overall scan map extent, D the dimension of the array, R the typical distance between the center of the array and the mid plane of the measured area and λ the acoustic wavelength. So the lowest frequency that this method could evaluate is 285 Hz according to the condition

$$f \gtrsim \frac{2cR}{DL_s}$$

A correction must also be provided to account for the apparent source displacement caused by the flow-convection effect. The apparent displacement is estimated as

$$\Delta = \frac{edU}{cR}$$

where d is the geometric distance between the microphone and the noise source and e is the thickness of flow crossed by the acoustic ray.

The whole setup and preliminary results have been described in detail by the authors [13]. The results are based on equivalent sound-power source maps produced by the algorithm. Typical maps shown in Fig. 8 and 9 show quantified contributions of LE and TE noise sources for both the baseline airfoil and the serrated flat-plate airfoil with $h/c_0 = 0.1$, and for specified frequency ranges. Integrating the two selected areas at the leading and trailing edges (red and green rectangular boxes respectively in Fig. 8-b), the contribution of each source defined as its integrated power is extracted, keeping in mind that the needed assumption of uncorrelated equivalent monopoles is believed a reasonable interpretation. The separation and extraction of individual noise sources is made possible only if the airfoil chord is non-compact, so that the equivalent sources at the trailing-edge and at the leading edge can be unambiguously separated. Here, compactness ends around ∼ 3.4 kHz, so the procedure is meaningful beyond this threshold. The main idea of the present work is to assess TIN reduction in the low-to-middle and the middle-to-high frequency ranges by complementary and totally different methods, namely spectra difference from far-field measurements for the former and source-power differences from microphone-array post-processing for the latter.
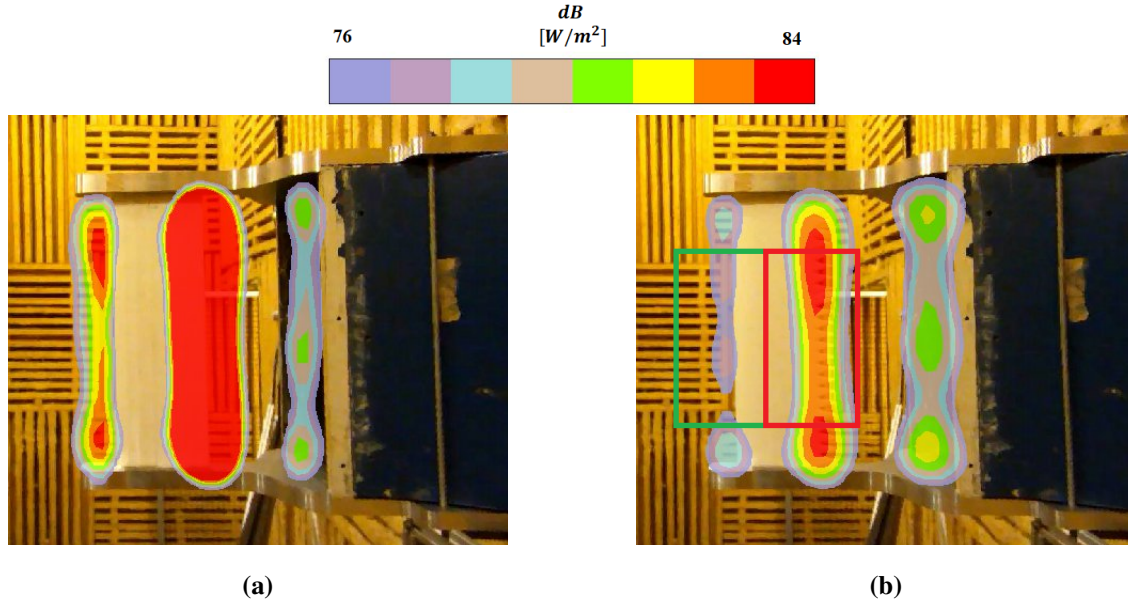
Fig. 8 Source localization color maps for the integrated frequency range $3.4 - 7.4$ kHz at 32 m/s. (a) baseline airfoil, (b) serrated airfoil with $h/c_0 = 0.1$. The rengtangular boxes define the interogation areas for the noise source extraction. Flow from right to left.

The maps in Fig. 8 indicate three contributions obviously attributed to leading-edge (LE) noise (identified to TIN), trailing-edge (TE) noise and background noise originating from the nozzle lips. The slightly different background-noise signature is not significant in terms of decibels. In contrast the more substantially different trailing-edge noise signatures with and without leading-edge serrations suggest that the latter notably modify the developing boundary layers. Figure 8 evidences reduction for both LE and TE emissions despite the fact that the noise reduction as assessed from the far-field results decreases beyond 4 kHz as shown in Fig. 5-a. Complementary maps are provided in Fig. 9 for the frequency ranges $[4.5 - 6.7]$ kHz and $[6.7 - 10]$ kHz. They confirmed that the background noise from the nozzle is kept unchanged. With leading-edge serrations, TEN is reduced in the range $[4.5 - 6.7]$ kHz and increased in the range $[6.7 - 10]$ kHz. The interpretation of these results is that the serrations reduce the large-scale content of the near-wall turbulence and at the benefit of the small-scale content.

10
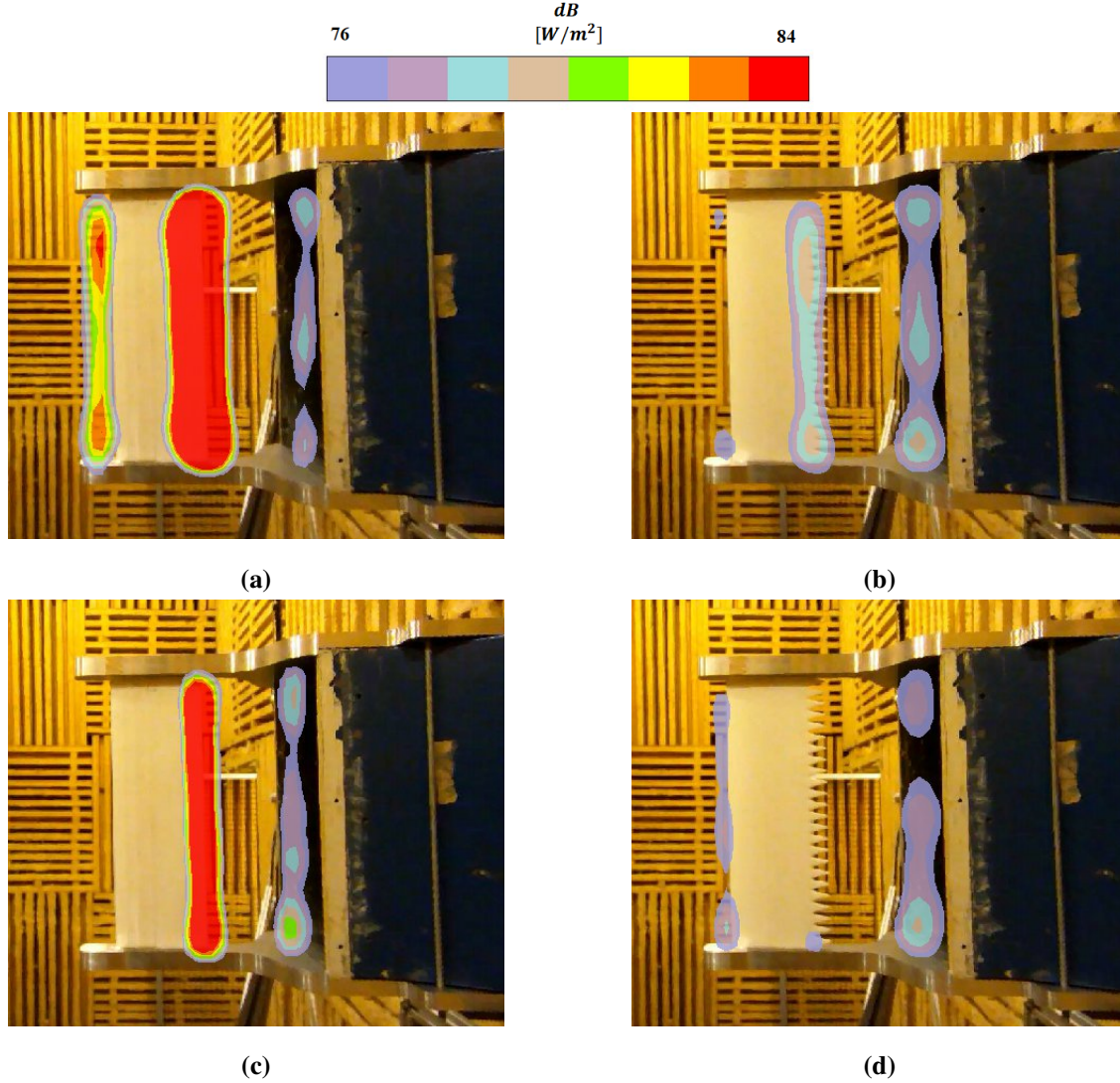
Fig. 9 Source localization maps in the integrated ranges $4.5 - 6.7\,kHz$ (a,b) and $6.7 - 10\,kHz$ (c,d), at $U = 32\,m/s$. (a,c): baseline airfoil; (b,d): serrated airfoil. Flow from right to left.

The results of map integration over the leading-edge (LE) and trailing-edge (TE) rectangular areas are displayed in Fig. 10 in integrated source-power (ISP) levels . The LE and TE power spectra are plotted as blue and red lines in Fig. 10-a and b for the baseline airfoil and the serrated airfoil, respectively, and the sum of both as the black lines. TE noise is much lower than LE noise below $4\,kHz$, which corresponds to the range in which both traces cannot be separated, therefore the erconstructed source spectrum only starts from this frequency. It is clear that TEN dominates at high frequencies for the serrated airfoil. The LE noise reduction as deduced from the difference of source-power spectra is plotted in red in Fig. 10-c, where it is compared to the reduction deduced from the far-field measurements, in blue. A monotonic increase, nearly linear in terms of decibles on a log-frequency scale, is found, up to the investigated high-frequency limit, with a maximum of about 15 dB. The overall noise reduction trend follows quite closely the function $10 log_{10}(f h/U) + 10$ proposed by Paruchuri *et al.* [5] for the optimum inclination angle of the serrations. Interestingly the blue and red reduction spectra coincide all along the validity range of the far-field subtraction procedure, which proves that both approaches produce estimates of the same quantity even though they totally differ in principle. The black line in Fig. 10-c attempts a reconstruction of the reduction that would be produced from the far-field data but taking the ISP levels as input, to test the consistency of the procedure. In other words a difference is made between the total spectra free of the background noise (combined TE and LE contributions) for both baseline and serrated airfoils. The discrepancies with the blue line are attributed to the background noise. The same black and blue spectra in

11

Fig. 10-c are reproduced in Fig. 10-d, in which the reduction spectrum of the trailing-edge noise only as deduced from the localization-map integration is added as the red line. The reduction remains positive up to a Strouhal number fh/U of 2 and is negative for higher Strouhal numbers. This illustrates the aforementioned increase and decrease in both frequency ranges in Fig. 9 and illustrates the different TE noise traces in Figs. 10-a and b.


(a)

(b)

(c)

(d)
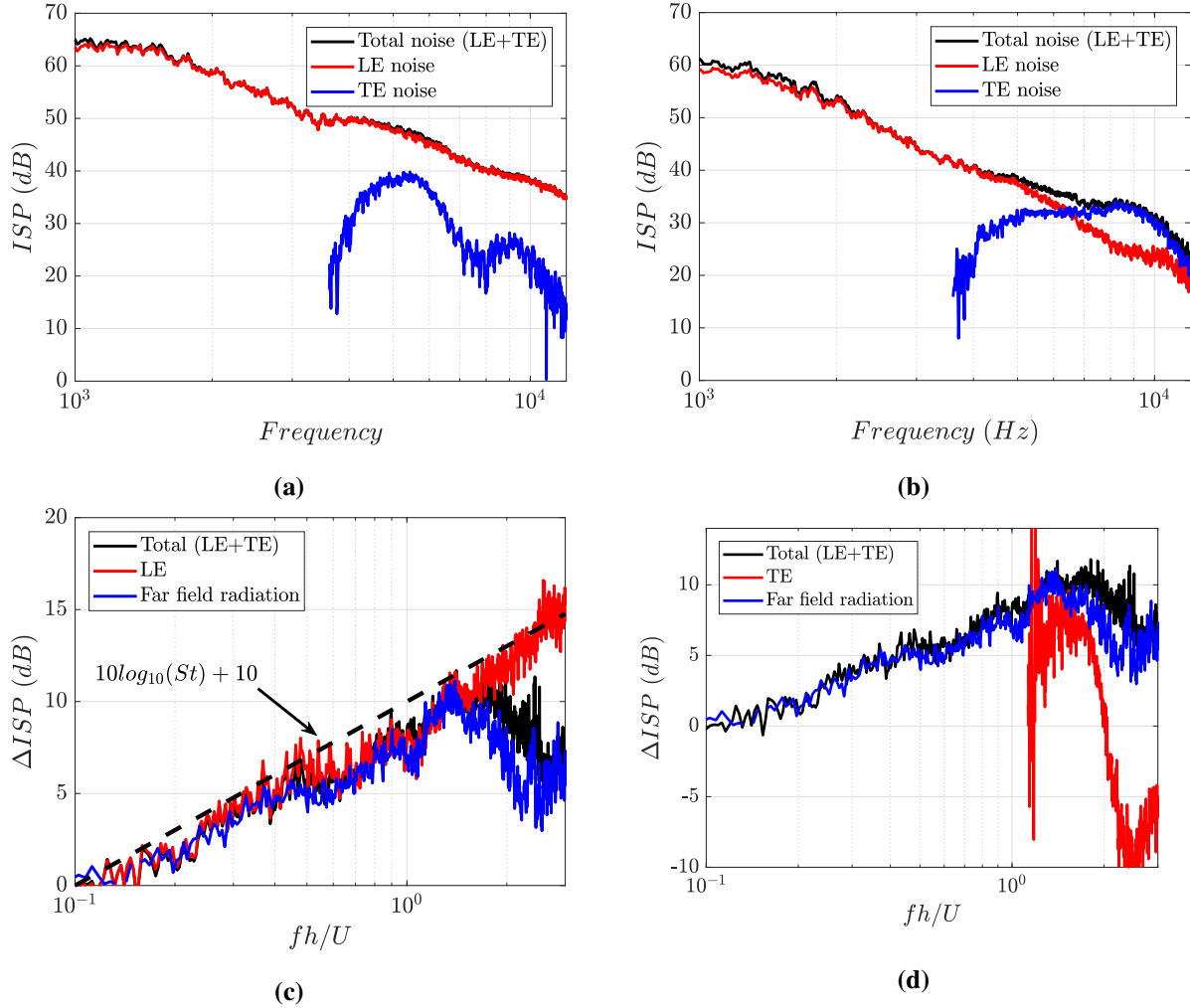
Fig. 10 LE noise (TIN), TE noise and total noise extractions generated by the filtered array processing (see the red and green interogated windows respectively in Fig. 8-b). (a): baseline airfoil; (b): serrated airfoil with $h/c_0 = 1$. (c): LE noise reduction as estimated from far-field data (blue) or map integration (red) and reconstruction of the far-field data processing from the map integration (black). (d): TE noise reduction from map integration.

IV. Flow Field Investigation

This section describes an ongoing work on the investigation of the three-dimensional features of the turbulence at the leading-edge with time-resolved tomographic particle image velocimetry (PIV) technique. Measurements are performed for flat-plate airfoils with both straight and wavy leading edges at zero angle of attack and the same geometrical parameters, mean chord and span. The time series of the three velocity components were recorded in a rectangular fuid volume. The measurements were carried out in the low-speed W-tunnel at Delft University of Technology. Smoke particles were injected into the flow and were illuminated by a laser sheet to allow the cameras to have a clear field of view in the flow field. The laser sheet is provided by a high speed *Continuum* Mesa PIV laser (Nd: YAG, 18 $mJ/pulse$ and given maximum power at 22V x 32A). Particle time slots were recorded by three high speed Photron Fastcam

APX-RS cameras (1024 x 1024 pixels, 12 *bit*, 20 $\mu m/px$) used with a Nikon-Nikkor 200 *mm* focal length, focus range $1 - 40$ and $f^{\#} = 11$. For each measurement, 10000 images were recorded at an acquisition frequency of $f_c = 10 \; kHz$. Cameras and laser were both synchronized and triggered by a LaVision HighSpeed contoller (HSC). The recorded images were post-processed with the software LaVision DaVis 8.1. Figure 11-a shows the corresponding PIV set-up consisted of three high-speed cameras, two poly-carbonate support plates and the laser beam. A metal grid made of flat rods was placed at the contraction outlet, generating nearly the same turbulent conditions as in the anechoic wind tunnel of ECL. The nozzle outlet cross section is 40 x 40 cm^2. The free-stream mean velocity was measured to be $U = 22 \; m/s$ using a Pitot tube and subsequently verified by the PIV results after the velocity field reconstruction. The final reconstructed measurement volume for the serrated version is approximately 30 x 20 x 10 mm^3 having the biggest side along the streamwise direction. The origin of the Cartesian coordinate system for each configuration is selected at the position of the mean chord at the mid-span plane of each model.


(a)   **(b)**
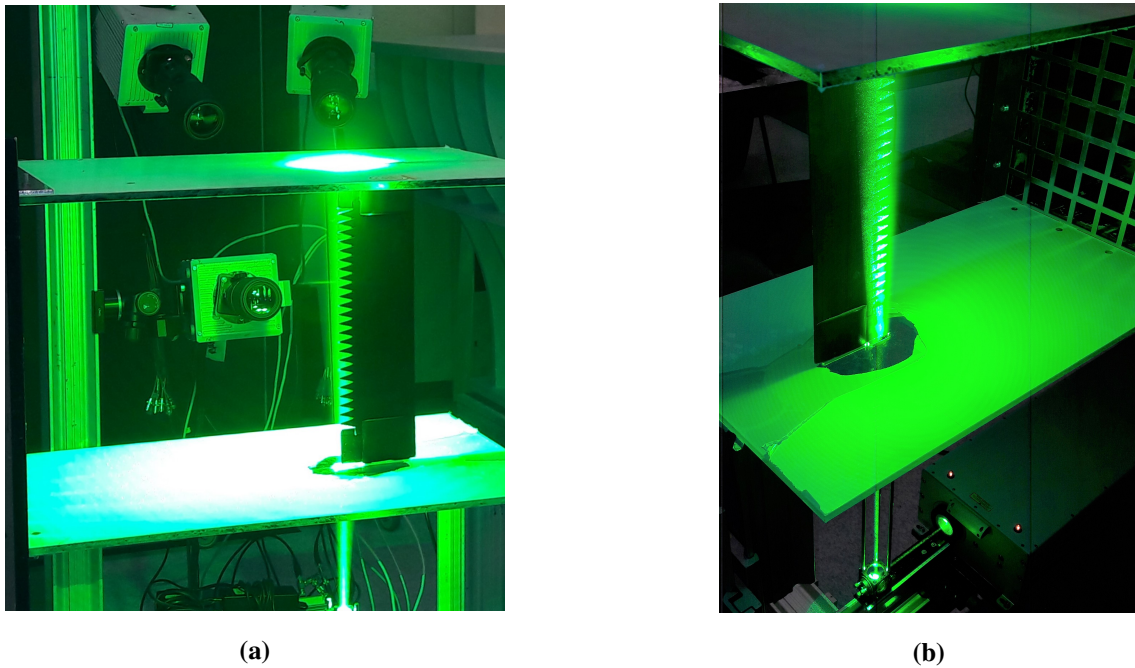
Fig. 11   Portside (a) and starboard (b) views of the tomographic PIV set-up, showing the serrated flat-plate airfoil held vertically and the laser beam along the spanwise direction. Turbulence grid seen on the right in (b).

The illuminated volume for PIV interrogation is shown in Fig. 12-a and the time-averaged velocity is visualized by orthogonal plane maps in three dimensions around the leading edge in Fig. 12-b for the serrated airfoil. Despite our best effort to reduce the contamination by light reflections on the wall, the very near-wall region remained inaccessible to the measurements. Eventually, the reconstructed volumes were located above the serrations parallel to the surface and the lowest recorded distance from the surface varies between 0.5 *mm* and 1 *mm*, which means that part of the boundary layer or whole is missing. The color map slices of the absolute velocity around the serrated leading-edge (Fig. 12-b) indicate a asymmetric flow on both sides of a tooth. The flow on the left-side part of the tooth decelerates whereas the velocity on the right-side remains closer to the free-stream velocity. The blockage of flow that would occur along the edge of a straight-edge airfoil appears mainly concentrated at the valleys of the serrations. Similar flow topology was observed by Avallone *et al.* [20] in the case of trailing-edge serrations. The flow tends to move into the empty spaces between adjacent teeth and to accelerate at their tips. Observations in latest studies by Turner and Chaitanya *et al.* [5, 21] mention the importance of the stagnation-point region for leading-edge noise and the deflection of the flow between the teeth. This raises the interest of paying attention to the vertical velocity component linked to the deflection of the flow around a tooth. The vertical velocity component W at different z positions above the surface are shown in Fig. 13, confirming the previous observations. Additionally, the thickness at the root of a tooth is larger than at the valley nearby. The vertical component upstream of the wavy leading edge and between teeth is nearly zero and goes to a maximum approaching the wall at a valley. This indicates that the vertical velocity component W is affected not only by

the surface thickness but also by the local transfer of flow.

(a)

(b)
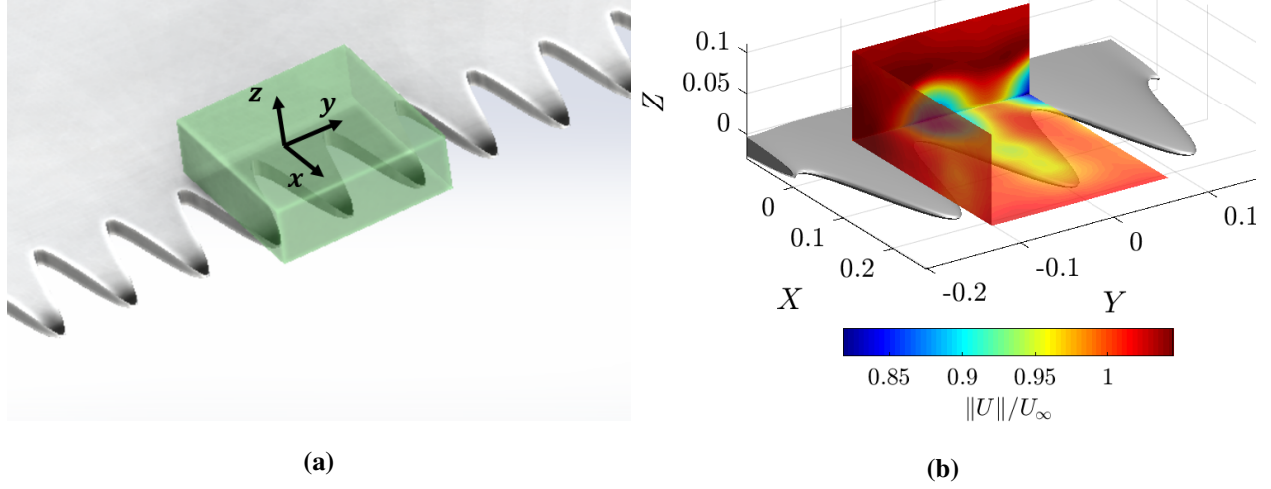
Fig. 12   Tomographic PIV domain. (a): illuminated volume; (b): complementary plane views of the dimensionless absolute velocity profile in the interrogation volume, with bottom plane along the span of the serrated airfoil at $z/c - 0 = 0.5 \ mm$. Flow speed $U = 22 \ m/s$.

(a)

(b)

(c)
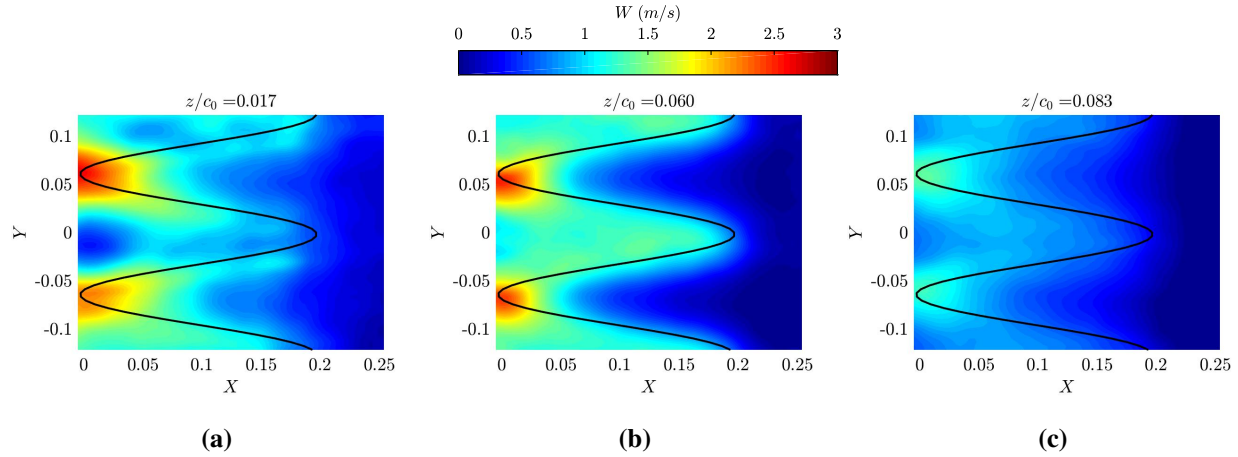
Fig. 13   Time-averaged velocity component $< W >$ on planes parallel to the $x - y$ plane for the serrated leading edge, at various z positions. (a): $z/c_0 = 0.017$, (b): $z/c_0 = 0.060$, (c): $z/c_0 = 0.083$. $U_\infty = 22 \ m/s$ is the free-stream mean velocity at the LE position ($x/c = 0.2$). Traces of the wavy pattern in the $x - y$ plane as black lines.

Contours of the mean velocity components along the serration tooth and the baseline straight-edge, projected in the horizontal $x - y$ plane, are shown in Fig. 14. Velocity contours in the planes $z/c_0 = 0.077$ and $z/c_0 = 0.052$ correspond to positions outside and very close to the boundary layer, respectively. The streamwise velocity component $< U >$ in Figs. 14-a and c follows a similar increase approaching the $x/c_0 = 0$ position as it is measured far from the boundary layer. The spatial velocity distribution of the vertical component $< W >$ for the straight edge features a sudden increase at the position of the leading edge ($x/c_0 = 0.2$) whereas the gradient of this component for the serrated edge is much lower, with smooth variations (subplots (a) and (b)). Fig. 12-a and Fig. 13-a visualize this flow topology which coincides with Avallone *et al.* [20] results regarding the spanwise component.

14
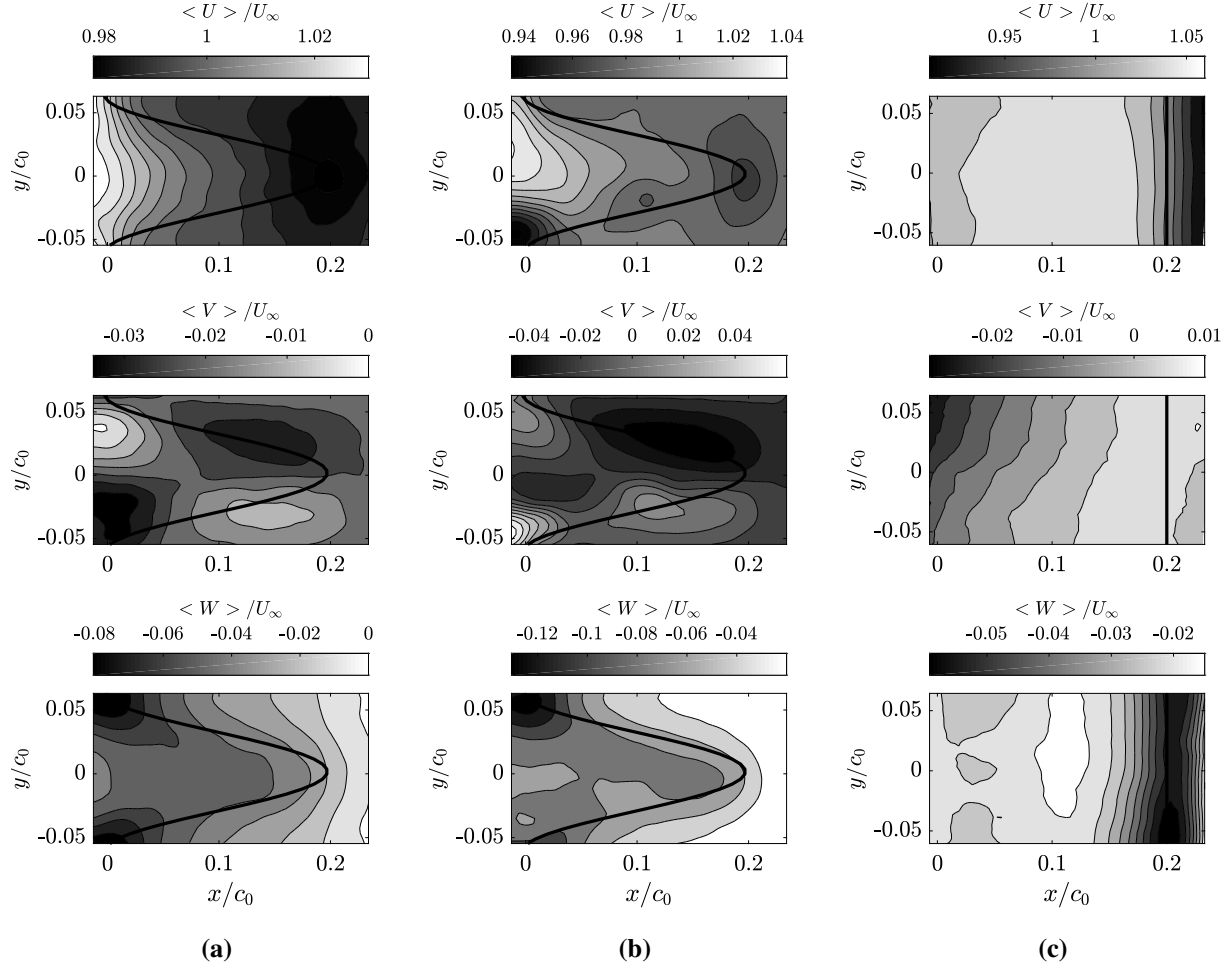
Fig. 14 Distributions of time-averaged velocity components $< U >, < V >, < W >$ along a tooth and corresponding baseline case at leading edge, in the $x - y$ plane. (a): $z/c_0 = 0.077$ and (b): $z/c_0 = 0.052$. Traces of the wavy serration pattern as black lines in subplots (a) and (b). (c): straight-edge result for $z/c_0 = 0.052$; projection of the straight line on the $x - y$ plane. $U_\infty = 22 \; m/s$ is the free-stream mean velocity at the LE position ($x/c_0 = 0.2$).

V. Conclusions

An experimental study on the turbulence-impingement noise reduction achieved by leading-edge serrations on flat-plate airfoils has been conducted. Previous investigations have been confirmed and completed by using various experimental techniques for the acoustic field and the flow patterns. In particular the effect of serrations has been studied off the mid-span plane, highlighting three-dimensional features. Apart from the reduction of sound levels, the typical directivity of turbulence-impingement noise (TIN) was found the same for both straight and wavy leading edges. This observation differs from the conclusions drawn by Lyu *et al.* [22] based on theoretical directivity pattern differences.

TIN reduction can be inferred from differences of far-field sound spectra as long as trailing-edge noise remains of much lower amplitude, which is the case only in a relatively low-to-medium frequency range. An alternative approach resorting to source-power spectra computed from microphone-array measurements has been shown to be more reliable at high frequencies for which turbulence-impingement noise is overwhelmed by trailing-edge noise (TEN). This allows demonstrating reductions of about $14 - 15dB$ with the single-sine serrations that could not be observed from the basic far-field investigation. Source-power spectra deduced from the localization technique have also shown that leading-edge serrations modify trailing-edge noise. TEN is reduced in the medium frequency range and increased in the high-frequency range. This is an additional point regarding to Chaitanya's *et al.* [5] observation that serrations at leading edge decrease airfoil self-noise in high frequencies because of boundary-layer modifications.

15

Preliminary results of time-resolved tomographic PIV give an insight into the three-dimensionality of the flow in the vicinity of the leading edge. Mean velocity visualization and characterization of the flow motion around the teeth, attest with a first analysis previous observations [5, 21] on the importance of the valley between the teeth as a source of noise generation. Maximization of the vertical components of the mean velocity at the valleys explains this steep change in direction motion and blockage of the flow reducing the norm of the velocity locally. Indeed, vertical disturbances are strongly linked with generation of sound according to Amiet's theory and assumptions. Further investigations will be provided by the authors to future studies according to the coherence and development of the turbulent flow along the serrations. The post-processing and interpretation of PIV results is still in progress.

Analytical modeling is also included in the research program. Amiet's theory has been successfully compared to the measurements in a complete three-dimensional context for the baseline/straight-edge airfoil. Equivalent predictions for a serrated airfoil will be attempted using Ayton & Kim's analytical model [17]. The aim is the definition of corrections that could be used in engineering context, after making extensive parametric use of the models.

Finally similar investigations are in progress with straight-edge porous NACA-0012 airfoils, for applications in which serrations could be more difficult to implement. Porosity is more suited for thick airfoils, increasing the benefit of thickness-induced TIN reduction by additional effects of local absorption. In both leading-edge strategies TEN remains another mechanism to deal with. Trailing-edge serrations 'tuned' to the boundary-layer parameters in the presence of leading-edge serrations appear as a best solution in this case.

Acknowledgments

References

[1] Roger, M., Schram, C., and De Santana, L., "Reduction of Airfoil Turbulence-Impingement Noise by Means of Leading-Edge Serrations and/or Porous Material," *19th AIAA/CEAS Aeroacoustics Conference*, 2013, pp. 1–20. doi:10.2514/6.2013-2108, URL http://arc.aiaa.org/doi/10.2514/6.2013-2108.

[2] Paruchuri, C., Subramanian, N., Joseph, P., Vanderwel, C., Kim, J. W., and Ganapathisubramani, B., "Broadband noise reduction through leading edge serrations on realistic aerofoils," *21st AIAA/CEAS Aeroacoustics Conference*, , No. June, 2015, pp. 1–29. doi:10.2514/6.2015-2202, URL http://arc.aiaa.org/doi/10.2514/6.2015-2202.

[3] Clair, V., Polacsek, C., Le Garrec, T., Reboul, G., Gruber, M., and Joseph, P., "Experimental and Numerical Investigation of Turbulence-Airfoil Noise Reduction Using Wavy Edges," *AIAA Journal*, Vol. 51, No. 11, 2013, pp. 2695–2713. doi: 10.2514/1.J052394, URL http://arc.aiaa.org/doi/10.2514/1.J052394.

[4] Roger, M., and Moreau, S., "Airfoil Turbulence-Impingement Noise Reduction by Porosity or Wavy Leading-Edge Cut : Experimental Investigations," *Inter-Noise 2016*, , No. 2, 2016, pp. 6006–6015.

[5] Chaitanya, P., Joseph, P., Narayanan, S., Vanderwel, C., Turner, J., Kim, J. W., and Ganapathisubramani, B., "Performance and mechanism of sinusoidal leading edge serrations for the reduction of turbulence-aerofoil interaction noise," *Journal of Fluid Mechanics*, Vol. 818, 2017, pp. 435–464. doi:10.1017/jfm.2017.141.

[6] Kim, J. W., Haeri, S., and Joseph, P. F., "On the reduction of aerofoil-turbulence interaction noise associated with wavy leading edges," *Journal of Fluid Mechanics*, Vol. 792, 2016, pp. 526–552. doi:10.1017/jfm.2016.95.

[7] Narayanan, S., Joseph, P., Haeri, S., Kim, J. W., Chaitanya, P., and Polacsek, C., "Noise reduction studies from the leading edge of serrated flat plates," *20th AIAA/CEAS Aeroacoustics Conference*, , No. June, 2014, pp. 1–14. doi:10.2514/6.2014-2320, URL http://www.scopus.com/inward/record.url?eid=2-s2.0-84903903591{\&}partnerID=tZOtx3y1.

[8] Narayanan, S., Chaitanya, P., Haeri, S., Joseph, P., Kim, J. W., and Polacsek, C., "Airfoil noise reductions through leading edge serrations," *Physics of Fluids*, Vol. 27, No. 2, 2015. doi:10.1063/1.4907798.

[9] Paruchuri, C. C., Narayanan, S., Joseph, P., and Kim, J. W., "Leading edge serration geometries for significantly enhanced leading edge noise reductions," *22nd AIAA/CEAS Aeroacoustics Conference*, , No. August, 2016. doi:10.2514/6.2016-2736, URL http://arc.aiaa.org/doi/10.2514/6.2016-2736.

[10] Chong, T. P., Biedermann, T., Koster, O., and Hasheminejad, S. M., "On the Effect of Leading Edge Serrations on Aerofoil Noise Production," *2018 AIAA/CEAS Aeroacoustics Conference*, 2018, pp. 1–24. doi:10.2514/6.2018-3289, URL https://arc.aiaa.org/doi/10.2514/6.2018-3289.

[11] Biedermann, T., Hintzen, N., Kameier, F., Chong, T. P., and Paschereit, C. O., "On the Transfer of Leading Edge Serrations from Isolated Aerofoil to Ducted Low-Pressure Fan Application," *2018 AIAA/CEAS Aeroacoustics Conference*, 2018. doi: 10.2514/6.2018-2956, URL https://arc.aiaa.org/doi/10.2514/6.2018-2956.

[12] Paruchuri, C., Joseph, P., and Ayton, L. J., "On the superior performance of leading edge slits over serrations for the reduction of aerofoil interaction noise," *2018 AIAA/CEAS Aeroacoustics Conference*, 2018, pp. 1–17. doi:10.2514/6.2018-3121, URL https://arc.aiaa.org/doi/10.2514/6.2018-3121.

[13] Bampanis, G., and Roger, M., "Three-dimensional effects in the reduction of turbulence-impingement noise of aerofoils by wavy leading edges," *Euronoise*, 2018, pp. 97–104.

[14] Roger, M., and Moreau, S., "Extensions and limitations of analytical airfoil broadband noise models," *International Journal of Aeroacoustics*, Vol. 9, No. 3, 2010, pp. 273–305. doi:10.1260/1475-472X.9.3.273, URL http://journals.sagepub.com/doi/10.1260/1475-472X.9.3.273.

[15] Roger, M., "On broadband jet-ring interaction noise and aerofoil turbulence-interaction noise predictions," *Journal of Fluid Mechanics*, Vol. 653, 2010, pp. 337–364. doi:10.1017/S0022112010000285.

[16] Moreau, S., Roger, M., and Jurdic, V., "AIAA 2005-2973 Effect of Angle of Attack and Airfoil Shape on Turbulence-Interaction Noise 11 th AIAA / CEAS Aeroacoustics Conference Meeting and Exhibit May 23-25 , 2004 / Monterey , California," *Manager*, , No. May, 2005, pp. 23 – 25. doi:10.2514/6.2005-2973.

[17] Ayton, L. J., and Kim, J. W., "An analytic solution for the noise generated by gust–aerofoil interaction for plates with serrated leading edges," *Journal of Fluid Mechanics*, Vol. 853, 2018, pp. 515–536. doi:10.1017/jfm.2018.583, URL https://www.cambridge.org/core/product/identifier/S0022112018005839/type/journal{_}article.

17

[18] Piet, J.-F., and G.Elias, "Modelisation du champ acoustique incident sur la coiffe d'ariane 5 par des sources simples," , 1994.

[19] Yakhina, G. R., Roger, M., Finez, A., Baron, V., Moreau, S., and Giez, J., "Broadband Airfoil-Noise Source Localization by Microphone Arrays and Modeling of a Swept Free-Tip Blade," 2018, pp. 1–14.

[20] Avallone, F., Pröbsting, S., and Ragni, D., "Three-dimensional flow field over a trailing-edge serration and implications on broadband noise," *Physics of Fluids*, Vol. 28, No. 11, 2016. doi:10.1063/1.4966633, URL http://dx.doi.org/10.1063/1.4966633.

[21] Turner, J. M., and Kim, J. W., "Aeroacoustic source mechanisms of a wavy leading edge undergoing vortical disturbances," 2017, pp. 582–611. doi:10.1017/jfm.2016.785.

[22] Lyu, B., and Azarpeyvand, M., "On the noise prediction for serrated leading edges," *Journal of Fluid Mechanics*, Vol. 826, 2017, pp. 205–234. doi:10.1017/jfm.2017.429.